Joule

CellPress

Article

Coupling of multiscale imaging analysis and computational modeling for understanding thick cathode degradation mechanisms

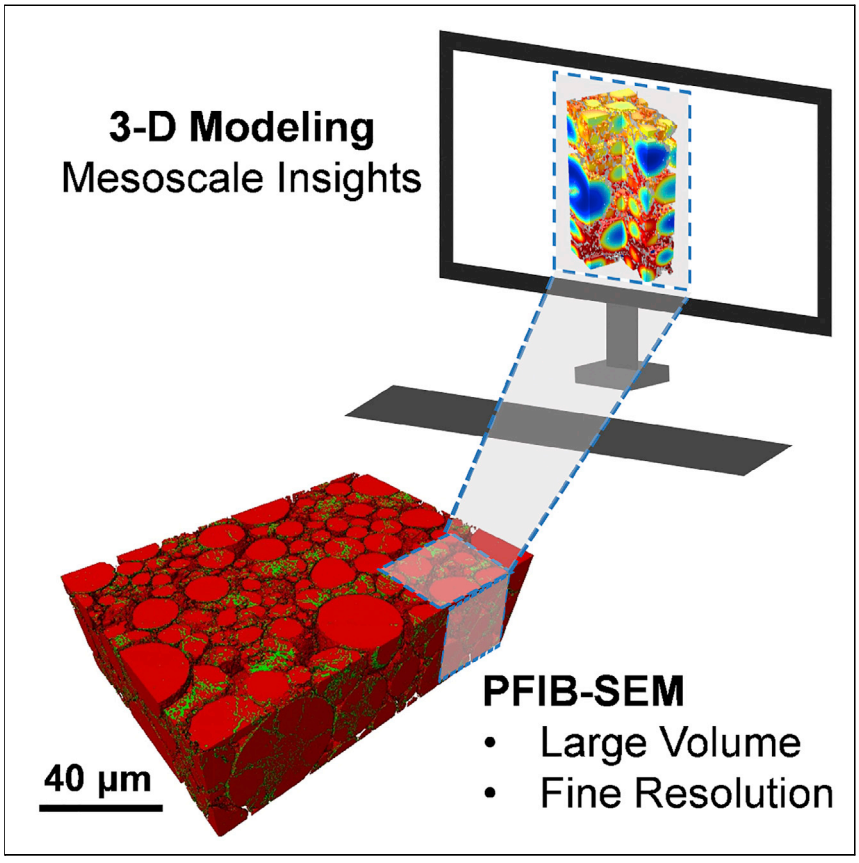

The understanding of lithium-ion batteries requires imaging capabilities able to provide information at a fine resolution over statistically relevant volume. With plasma focused ion beam-scanning electron microscopy (PFIB-SEM), the whole electrode can be resolved in 3D with a resolution of few nm. Here, this technology is applied to a thick positive electrode to investigate the degradation mechanism during the cycling of the cell. Coupled with modeling, it provides quantitative insights on the evolution of the structure of the thick electrode.

Minghao Zhang, Mehdi Chouchane, S. Ali Shojaee, ..., Herman Lemmens, Alejandro A. Franco, Ying Shirley Meng

alejandro.franco@u-picardie.fr (A.A.F.)
shirleymeng@uchicago.edu (Y.S.M.)

Highlights

PFIB allows the 3D imaging of large volumes relevant for statistical analyses

Information at both the nanoscale and microscale can be obtained in a timely manner

Particles cracking and contact loss in thick electrode result in degradation

The non-uniform CEI will accentuate the heterogeneities over long cycling

Zhang et al., Joule 7, 1–20
January 18, 2023 © 2022 Elsevier Inc.
https://doi.org/10.1016/j.joule.2022.12.001

Please cite this article in press as: Zhang et al., Coupling of multiscale imaging analysis and computational modeling for understanding thick cathode degradation mechanisms, Joule (2022), https://doi.org/10.1016/j.joule.2022.12.001

Joule

CellPress

Article

Coupling of multiscale imaging analysis and computational modeling for understanding thick cathode degradation mechanisms

Minghao Zhang,[1,8] Mehdi Chouchane,[2,3,8] S. Ali Shojaee,[4] Bartlomiej Winiarski,[4] Zhao Liu,[4] Letian Li,[4] Rengarajan Pelapur,[4] Abbos Shodiev,[2,3] Weiliang Yao,[1] Jean-Marie Doux,[1] Shen Wang,[1] Yixuan Li,[1] Chaoyue Liu,[2,3] Herman Lemmens,[4] Alejandro A. Franco,[2,3,5,6,*] and Ying Shirley Meng[1,7,9,*]

SUMMARY

Using a thick NMC811 ($LiNi_{0.8}Mn_{0.1}Co_{0.1}O_2$) electrode as an example, we present a macro- to nanoscale 2D and 3D imaging analysis approach coupled with 4D (space + time) computational modeling to probe its degradation mechanism in a lithium-ion battery cell. Particle cracking increases and contact loss between particles and carbon-binder domain are observed to correlate with the cell degradation. This study unravels that the reaction heterogeneity within the thick cathode caused by the unbalanced electron conduction is the main cause of the battery degradation over cycling. The increased heterogeneity in the system will entail more cathode regions where the degree of active material utilization is uneven, leading to higher probabilities of particle cracking. These findings shed light on the crucial role of the electronic and ionic transportation networks in the performance deterioration of the thick cathode. They also provide guidance for cathode architecture optimization and performance improvement.

INTRODUCTION

Li-ion batteries (LIBs) have dominated today's battery technologies for application in portable electronic devices due to their high specific energy density, wide working temperature, and long cycle life. A surge in LIBs production over the last 10 years has driven down the prices to the point that utility-scale storage (in kilowatt-hours magnitude) such as electric vehicles and residential systems became commercially viable. At present, the energy density of the mass-produced LIBs system is around 200–250 Wh/kg at the cell level (650–800 Wh/kg at the cathode material level). However, the energy density of current LIB cells will not be able to meet the ever-growing demand of electric vehicle energy-storage market in the future. The short term expectation of the automotive field is 350 Wh/kg while the long-term goal is as high as 500 Wh/kg at the cell level with a life cycle over 1,000 times.[1] Among all the practical approaches to build the highest specific energy cells, increasing the active material loading amount and the composite electrode thickness is a promising option, which in turn reduces the contents of the inactive components (current collectors, separators, and packaging) per stack volume and provides reduced cell manufacturing costs. As shown in Figure S1, the cell specific energy can be further optimized to over 350 Wh/kg by increasing the cathode thickness to ca. 100 μm with similar porosity. However, when the cathode thickness is larger than 50 μm, establishing an efficient transport pathway for both lithium-ion and electrons becomes

CONTEXT & SCALE

The lithium-ion battery is a complex system whose electrode thickness ranges from a few tens to several hundred micrometers and consists of components that can be nanosized. This makes it difficult to capture both the structure of the nanosized particles and the volume of the electrode significant enough for statistical purposes. Classical methods such as computed tomography or focused ion beam-scanning electron microscopy (FIB-SEM) lack either the volume resolved or the resolution.

Plasma focused ion beam-scanning electron microscopy (PFIB-SEM) enables fast-milling, hence a larger resolved volume compared with FIB-SEM. This method is applied to a thick positive electrode, allowing to resolve the 3D structure of the whole thickness. The electrodes before and after cycling are compared to highlight the structural evolution and degradation mechanisms. The experimental observations are complemented with modeling insights built from the resolved electrode.

more challenging.[2,3] The induced kinetic limitations in the composite thick electrode can retard the reaction in some regions of the electrode, which leads to electrode degradation due to operation inhomogeneity.[4]

To systematically study and quantify the structural and chemical evolution of composite electrodes during electrochemical cycling, a multiscale imaging and analysis approach is highly desirable.[5] This is because the degradation process of the thick electrode is closely associated with structural and chemical complexities at different length scales. Full 3D characterization is required when evaluating complex morphologies and interconnectedness nature of different components in thick electrodes including pores, active material, carbon additive, and binder. Detailed 3D structural and chemical information about the thick electrode is also critical to quantify and model the inhomogeneity. Non-destructive techniques such as X-ray computed tomography (CT) and nuclear magnetic resonance imaging (MRI) offer 3D imaging capabilities. For instance, Lu et al. revealed how the performance of LIBs can be affected by microstructural heterogeneities under high-rate conditions using a nano-CT dual-scan superimposition technique.[6] These techniques are limited in either spatial resolution or imaging contrast to differentiate carbon-binder domain (CBD) from pores.[7,8] Consequently, imaging across multiple length scales often relies on electron microscopy to provide 3D information at microscale and nanoscale.[9,10]

Focused ion beam-scanning electron microscopy (FIB-SEM) is an analytical method that combines an ion beam for materials processing and an electron column for imaging.[11] It enables both 2D and 3D imaging capabilities with nm spatial resolution, which is an effective analytical approach for the LIB electrode structure. To date, conventional Ga^+ FIB-SEM has been widely employed for battery materials including interface/interphase characterization, 3D quantification, and computational simulation-based analysis.[12,13] However, Ga^+ FIB material's removal efficiency limits its capability to access representative areas and volumes in some battery components, e.g., electrodes with thicknesses of hundreds of microns.[11]

The emerging plasma FIB-SEM (PFIB-SEM) technology has recently been developed with different ion sources and high removal efficiency.[14,15] Compared with Ga^+, the liquid metal ion source suffers from spherical aberration at high current range, which is not suitable for large area and volume millings,[11] while the plasma ion source is broader but collimated, making the attainment of currents in the μA range possible.[14] Thus, PFIB-SEM technique promises great potential for battery materials characterization, due to accessing representative 2D areas and 3D volumes via ~40 times faster milling rate than the Ga^+ systems (Figure 1A). In addition, PFIB-SEM enables Ga^+-free sample preparation on advanced battery systems through non-reactive ion sources (Xe^+ and Ar^+ ion).

Recently, PFIB-SEM has been applied in the battery field to study interphase stability between the electrode and the solid/liquid electrolyte.[16–18] Gong et al. applied PFIB cutting coupled with secondary ion mass spectroscopy to confirm the formation of a fluoride-rich interphase after adding a fluoroethylene carbonate additive in the organic electrolyte, which yields a denser Li metal structure during the electrochemical deposition process.[18] PFIB-SEM was also used in solid-state batteries to demonstrate the interphase stability between the solid electrolyte and deposited lithium metal after long-term cycling.[17] Both prior works lack of quantitative analyses on the interphase stability during the electrochemical cycling. To date, PFIB-SEM's full capabilities and applications, especially for 3D imaging and quantification, have not yet been reported in the archival literature for battery research.

[1]Department of NanoEngineering, University of California San Diego, La Jolla, CA 92093, USA

[2]Laboratoire de Réactivité et Chimie des Solides (LRCS), UMR CNRS 7314, Université de Picardie Jules Verne, Hub de l'Energie, 80039 Amiens Cedex, France

[3]Réseau sur le Stockage Electrochimique de l'Energie (RS2E), FR CNRS 3459, Hub de l'Energie, 80039 Amiens Cedex, France

[4]Thermo Fisher Scientific, 5350 NE Dawson Creek Drive, Hillsboro, OR 97124, USA

[5]ALISTORE-European Research Institute, FR CNRS 3104, 80039 Amiens Cedex, France

[6]Institut Universitaire de France, 103 Boulevard Saint Michel, 75005 Paris, France

[7]Pritzker School of Molecular Engineering, University of Chicago, Chicago, IL 60637, USA

[8]These authors contributed equally

[9]Lead contact

*Correspondence: alejandro.franco@u-picardie.fr (A.A.F.), shirleymeng@uchicago.edu (Y.S.M.)

https://doi.org/10.1016/j.joule.2022.12.001

Please cite this article in press as: Zhang et al., Coupling of multiscale imaging analysis and computational modeling for understanding thick cathode degradation mechanisms, Joule (2022), https://doi.org/10.1016/j.joule.2022.12.001

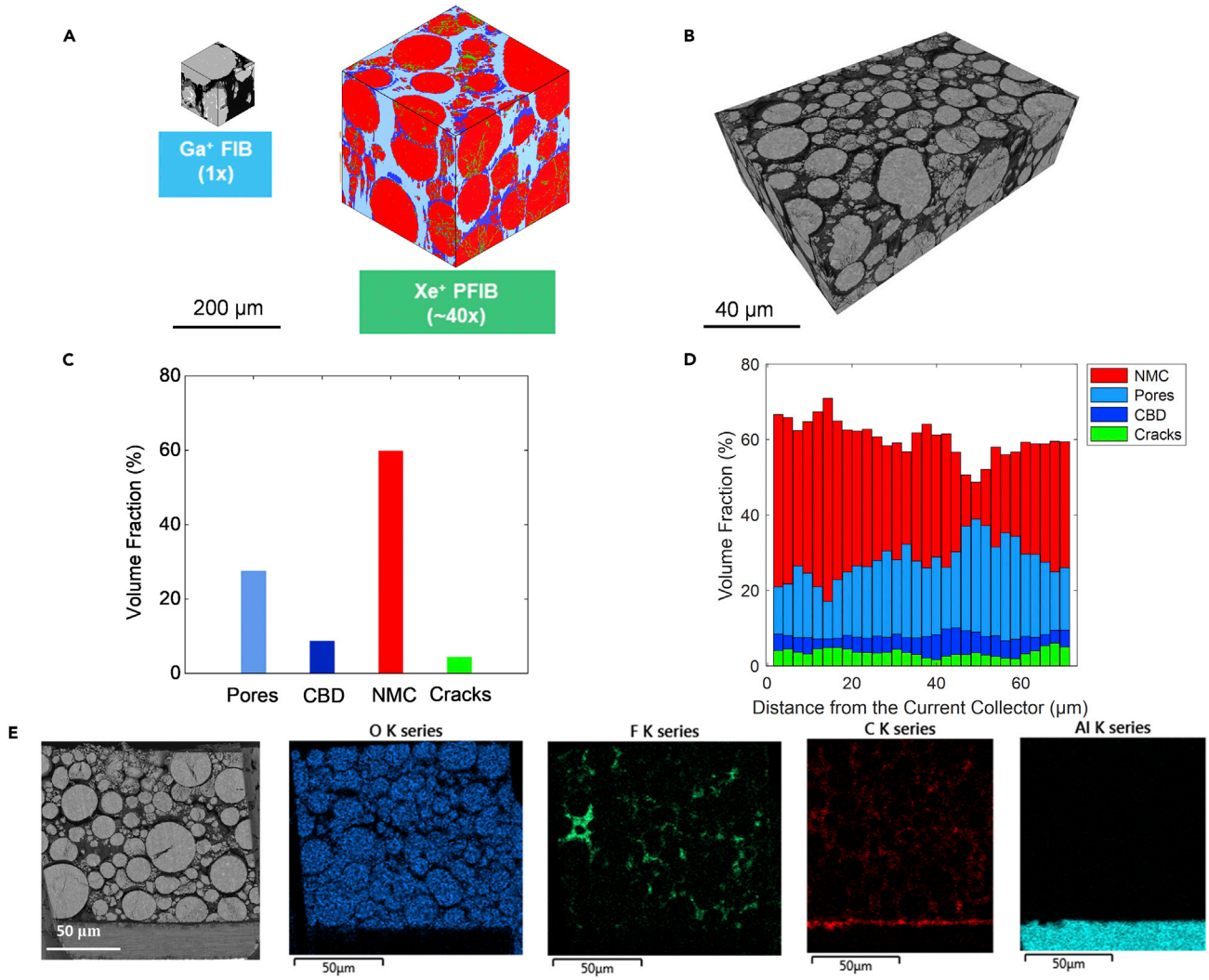

Figure 1. 3D quantitative analysis of NMC811 thick electrode via PFIB

(A) Schematic image of the emerging PFIB technology developed with different ion sources and high removal efficiency.

(B) 3D reconstruction of pristine NMC811 thick electrode using the sliced images collected via PFIB.

(C and D) The quantified volume fraction of different components in the reconstructed volume after pore-back correction and segmentation (C) and the spatial distribution of each component along the electrode thickness direction (D).

(E) The SEM image and energy-dispersive X-ray spectroscopy (EDX) mapping on a 2D cross-section of NMC811 thick electrode.

The aim of this work is to investigate the mechanism of thick electrode degradation by a multiscale imaging approach. A cell made of a high Ni layered NMC811 ($LiNi_{0.8}Mn_{0.1}Co_{0.1}O_2$)-based cathode (~80 μm in thickness, ~6 mAh/cm^2 in areal capacity) and a Li metal anode was selected in this study as a representative example of the ongoing research target (more than 400 Wh/kg energy density at the cell level) in the battery community.[19] PFIB-SEM was applied to access large representative 3D volumes (>100 × 35 × 70 μm^3) to assess the microstructure evolution of the thick NMC811 cathode under different electrochemical cycling conditions. In order to gain insights on the reaction heterogeneity along the thickness direction at the nanoscale, lamellas from both the top and bottom locations of the NMC811 electrodes were prepared by the FIB lift-out process for scanning transmission electron microscopy (STEM) down to atomic resolution. The micro and nano structural characteristics extracted from this multiscale imaging approach were used to build a 4D

Please cite this article in press as: Zhang et al., Coupling of multiscale imaging analysis and computational modeling for understanding thick cathode degradation mechanisms, Joule (2022), https://doi.org/10.1016/j.joule.2022.12.001

(space + time) computational model based on the 3D PFIB data collected at the electrode scale, accounting for the explicit location of active material, CBD, and pores. Furthermore, this model allows assessing the impact of the cathode electrolyte interphase (CEI) formation on the transport properties, as well as identifying spatial operation heterogeneities inside the thick electrode. This study, supported on an experimental/modeling synergy, reveals the crucial role of CBD in defining the electronic and ionic transportation networks of the thick cathode. These networks greatly affect the operation heterogeneity and electrode performance under high voltage cycling conditions. Building on these insights, we demonstrate a high voltage LNMO ($LiNi_{0.5}Mn_{1.5}O_4$)-based cathode (~80 μm in thickness) that can deliver stable cycling performance thanks to a CBD percolation network optimized through the dry electrode coating process.

RESULTS AND DISCUSSION

Three-dimensional imaging and quantification of thick electrode via PFIB-SEM

Figure 1B shows the 3D rendering volume (108 × 33 × 72 μm^3) of the pristine NMC811 using the sliced images collected via PFIB. The following image segmentation and reconstruction for all the samples were performed in this size to exclude the current collector and other unrelated regions in the image. The final volume fractions of each component in the pristine sample after pore-back correction are 29% pores space, 9% CBD, 58% NMC particles, and 4% cracks within the NMC particles. These results are in line with the expected pores volume percentage from the sample production (20–30 vol %).

Ideal thick electrode processing should produce smooth lamination with uniform distribution of each component along the thickness direction to prevent local deviations from the target state of charge/discharge (SOC/SOD). The large, reconstructed 3D volume obtained from PFIB technique provides an opportunity to quantitively evaluate the quality of the pristine thick electrode sample, which in turn will offer feedback on parameters optimization of the manufacturing process. As shown in Figure 1D, CBD distributes evenly along the thickness direction, enabling an intact transport network for both Li^+ ions and electrons. The even distribution of CBD is further confirmed by energy-dispersive X-ray spectroscopy (EDX) mapping (Figure 1E) on one serial section obtained from PFIB cutting. No major segregation of carbon additive and fluorinated polymer binder is observed in C and F element mapping, respectively. The thin carbon-rich layer on top of Al current collector is designed to facilitate electron transport at the electrode/current collector interphase for an improved rate capability.

Unlike the uniformly distributed CBD phase, the volume fraction of NMC particles deviates from the average value at ~50 μm from the current collector. The opposite distribution trend for the particles and pores component indicates that the density of the active materials varies along the thickness direction. It is important to note that the intergranular cracking within the secondary particles can be introduced even from the pristine state by the electrode calendering process. To confirm the calendering effect, the PFIB cutting and 3D analysis were also performed on the raw NMC811 powders. The cross-sections (Figure S2) were segmented using a three-component watershed segmentation since no CBD was involved in the powder sample. Following the similar imaging segmentation process, the crack vol % within raw powders were estimated to be less than 1% (~0.12%). To avoid particle density variance from different samples, the quantified volume fraction of cracking is normalized by the volume of secondary particles for each sample when comparing the effects of

Please cite this article in press as: Zhang et al., Coupling of multiscale imaging analysis and computational modeling for understanding thick cathode degradation mechanisms, Joule (2022), https://doi.org/10.1016/j.joule.2022.12.001

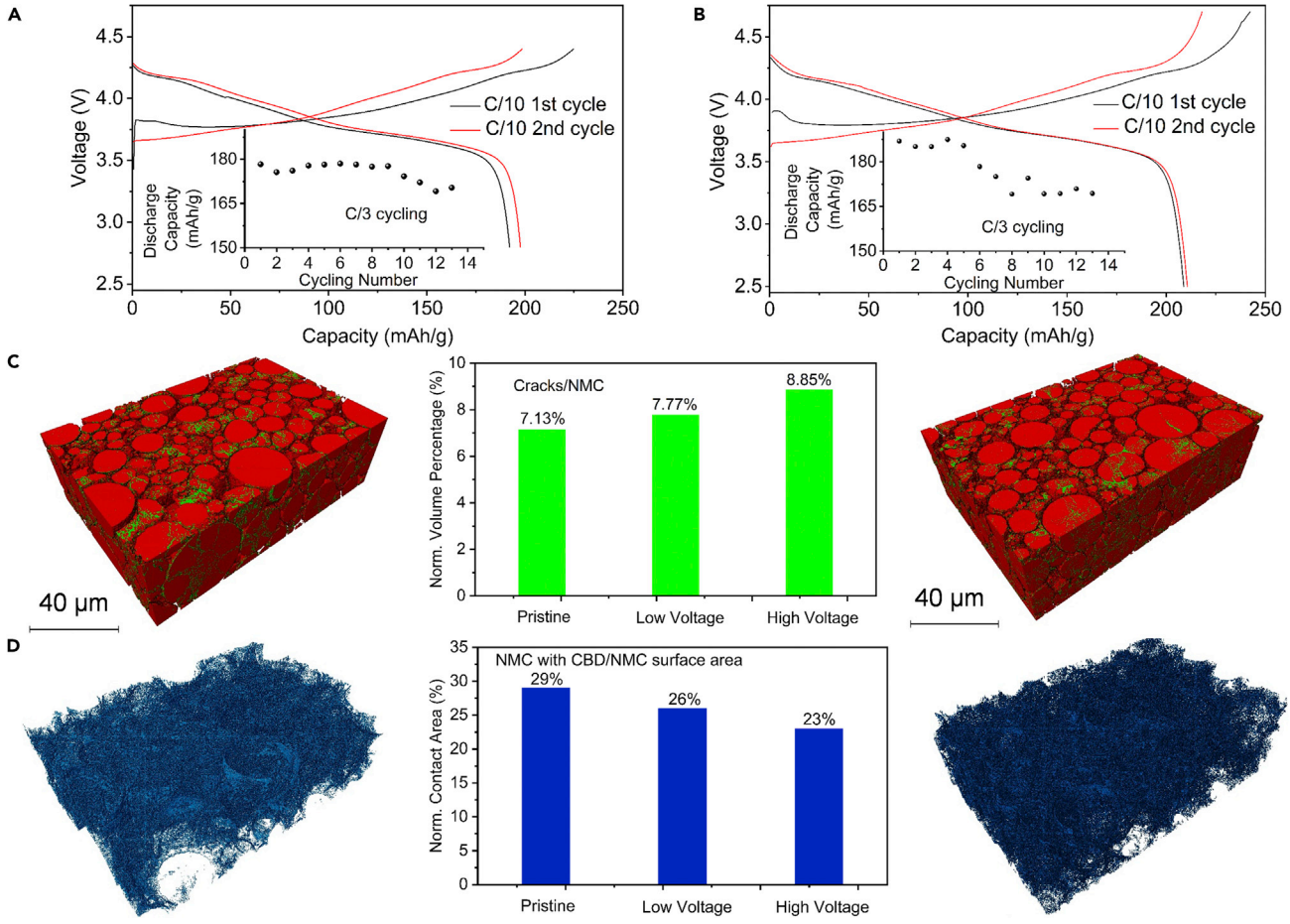

Figure 2. Microstructure degradation quantification of NMC811 thick electrode during electrochemical cycling

(A and B) Voltage profiles and cycling performance of NMC811 thick electrode in half-cell with different voltage cutoffs, between 4.4 and 2.8 V (A), between 4.7 and 2.5 V (B).

(C) The reconstructed 3D volume and quantified cracking volume percentage of NMC811 thick electrode after cycling between 4.4 and 2.8 V (left), between 4.7 and 2.5 V (right) (green, cracks; red, NMC particles).

(D) The reconstructed and quantified contact surface areas between NMC particles and CBD component after cycling between 4.4 and 2.8 V (left), between 4.7 and 2.5 V (right). To avoid particle density variance from different samples, the quantified number in (C) and (D) is normalized by the total volume or surface area of the particles.

cycling in the following text. Although the calendering is necessary to increase the volumetric energy density, the comparison between the powder and pristine electrode indicates a large amount of particle cracking can be introduced during the calendering process via uniaxial pressure.

Electrode structure degradation revealed by multiscale imaging

The pristine NMC811 thick electrode was then paired with the Li metal anode to study the electrode structure evolution under different cycling conditions. By applying unlimited Li inventory with flooded amount of carbonate electrolyte in the electrochemical testing, the cell performance degradation can be reasonably correlated with the cathode structure changes. As shown in Figures 2A and 2B, the NMC811 half-cell cycled with charging voltage up to 4.4 V delivers a capacity retention of 96% after 15 cycles. Although the cell with higher cutoff voltage (4.7 V) shows a larger initial capacity at both C-rates (209 versus 192 mAh/g at the C/10-rate, 187 versus 178 mAh/g at the C/3-rate), nearly 10% of the capacity loss

Please cite this article in press as: Zhang et al., Coupling of multiscale imaging analysis and computational modeling for understanding thick cathode degradation mechanisms, Joule (2022), https://doi.org/10.1016/j.joule.2022.12.001

is observed within the first 15 cycles. High-voltage-induced capacity degradation in layered oxide cathode is well documented in previous studies. Surface reconstructions to spinel/rock-salt-type structure have been widely observed in NMC cathodes after electrochemical cycling,[20,21] which can impede 2D diffusion pathway of Li ions in the phase transformation regions. In addition, the upper stable operating voltage for carbonate-based organic electrolyte is generally limited to 4.5 V versus Li^+/Li.[22] When the voltage increases further, electrolytes decompose and fail to form an effective passivating layer on the cathode particle surface, which deteriorates the battery cycling stability.[23]

Mechanical degradation has been qualitatively observed in NMC materials using SEM and TEM,[24] including cracks within secondary particles similar to those observed in the pristine electrode. Due to Ga^+ ion FIB cutting limitations, the intergranular cracks can be only revealed in several particles, which is insufficient to provide a statistically significant comparison between the cathode sample at the cycled and pristine state. More importantly, quantitative analysis of mechanical degradation in NMC materials based on large volumes has not yet been achieved using conventional Ga^+ FIB-SEM. In our work, the intergranular cracking volume percentage in the NMC811 thick electrode after cycling under different conditions can be well quantified using the large, reconstructed 3D volume, as shown in Figures 2C and S3. After 15 cycles under lower voltage cutoff, the cracking volume percentage increases relatively by 9%. While for the cathode exposed to 4.7 V, the cracking relative increase is nearly three times larger, by 24% compared with the pristine state. This difference is not surprising considering the larger anisotropic volume expansion of the primary grains at higher SOC.[25] As cracks keep developing, the electrolyte penetrates deeper to damage the interior grains through the corrosion effect under the high voltage condition, which can finally lead to dead grains with loss of electronic contact. This quantification on cracking volume evolution manifests one of the electrode degradation mechanisms, and highlights that this phenomenon will be amplified under high voltage cycling conditions. It should be noted that extensive cracking has been observed in NMC811 cathodes cycled with the carbonate electrolyte after hundreds of cycles,[26] and the intergranular cracking between primary grains can be suppressed or delayed by employing suitable additives or electrolytes.[26]

Recently, gradual failure of the fluorinated polymer binder has been reported owing to its incompatibility with high voltage operation, resulting in the contact loss at both the electrode/current collector interface and surface of the cathode particles.[27] In this work, the contact surface area changes between NMC particles and CBD were also quantified for different samples (Figure 2D). Compared with the pristine electrode, the surface contact area decreases relatively by 10% and 20% for the low-voltage and high-voltage cycling, respectively. This gradual loss of conductive networks and mechanical strength in the thick electrode due to less contact area between NMC particles and CBD can be detrimental for long-term cycling stability, which is neglected in previous characterization studies. The physical performances of different binders[28] have a significant impact on the adhesion of different components inside the electrode and this impact is undoubtedly amplified under the condition of high voltage operation.[27] For high voltage cycling, it is critical to choose the proper binder and conductive agent to prevent electrode delamination and enable favorable transport properties.

With the PFIB data analysis at the macroscale, no clear trend of microstructural evolution along the thickness direction is observed in the reconstructed volume

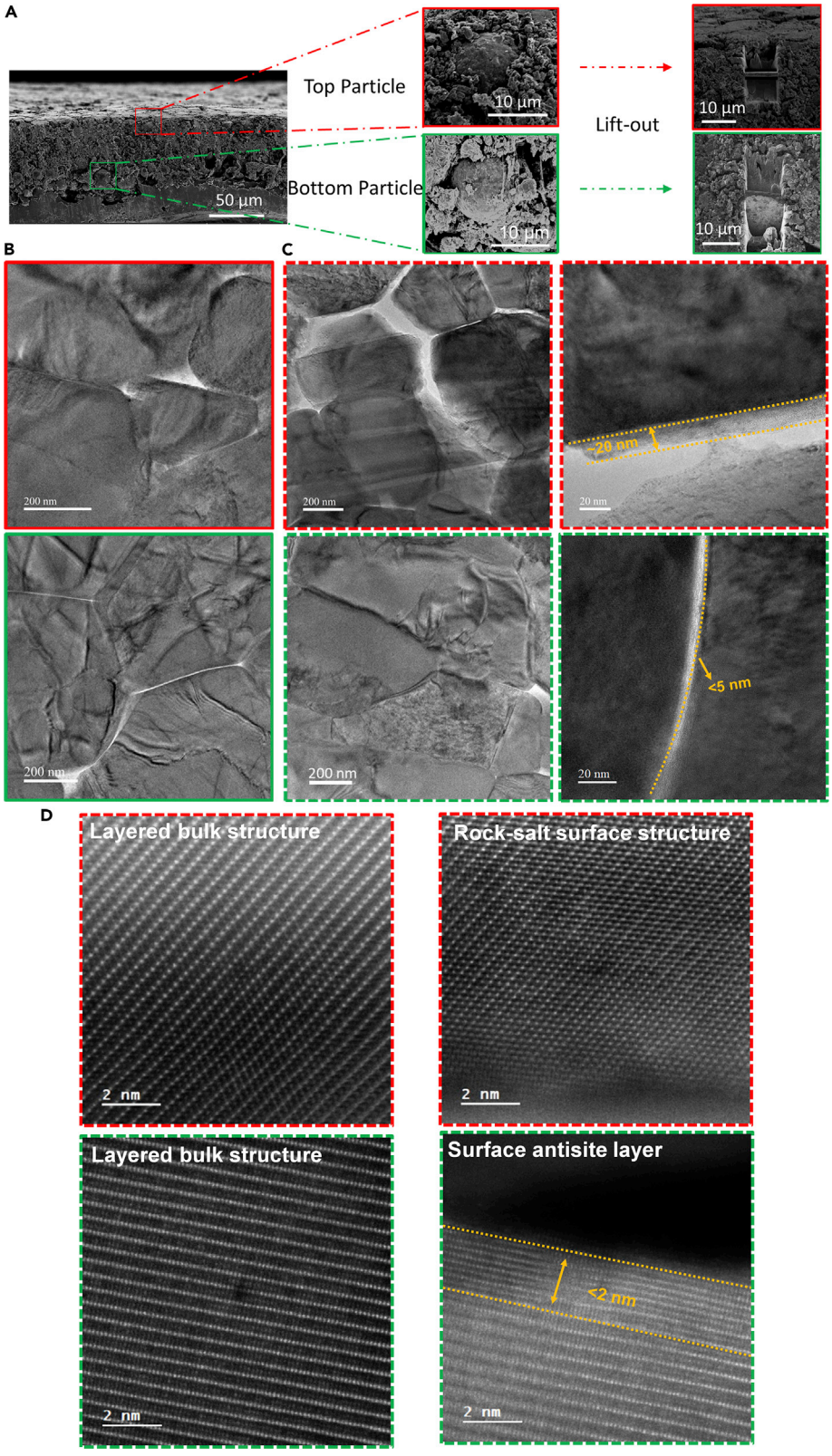
A
Top Particle
Bottom Particle
50 μm
10 μm
10 μm
Lift-out
10 μm
10 μm
B
C
200 nm
200 nm
20 nm
200 nm
200 nm
20 nm
<5 nm
D
Layered bulk structure
2 nm
Rock-salt surface structure
2 nm
Layered bulk structure
2 nm
Surface antisite layer
<2 nm
2 nm

Figure 3. Thick electrode degradation analysis at the nanoscale via analytical cryogenic TEM

(A) Cross-section images of top and bottom locations from the thick NMC811 electrode for FIB lift-out process.

(B) TEM images of the top and bottom lamella sample from pristine NMC811 electrode.

(C) HRTEM images of the top and bottom lamella sample from NMC811 electrode after cycling between 4.7 and 2.5 V.

(D) Atomic resolution HAADF images of the top and bottom lamella sample for single particle bulk and surface region after cycling between 4.7 and 2.5 V (images with red frame, top lamella; images with green frame, bottom lamella).

for the cycled NMC811 electrodes (Figure S4). In order to study the impact of kinetic limitations on the thick electrode performance, further analysis at the nanoscale is thus performed. Lamellas from both the top and bottom locations of the thick electrode were prepared by the FIB lift-out process, as shown in Figure 3A. The prepared lamellas were then thinned down to ~100-nm thick for (S)TEM-EDX characterizations, and the morphology of the lamella is shown in Figure 3A. To protect the thin surface layer from electron dose damage, all the high resolution TEM (HRTEM) images were recorded under cryogenic temperature, following our sample transfer and imaging protocols.[29] As shown in Figure 3B, the primary grains in the pristine electrode are in close contact and exhibit clear grain boundaries with the crystalline phase contrast. No obvious difference is noticed for the primary grains from different locations of the thick electrode.

After electrochemical cycling under high voltage, a larger separation among the primary grains appears in the top lamella sample compared with the bottom location of the thick electrode (Figure 3C). An ununiform amorphous layer is identified on the surface of the primary grains. This amorphous layer is around 20-nm thick and is located on the grains near the separator (top lamella), which is four times thicker than that from the bottom location. EDX phosphorus mapping results in Figure S5 clearly indicate that the amorphous layer contains electrolyte decomposition products, which can be referred as CEI. The thicker CEI formation on the grains near the separator can result from the excess electrolyte amount stored in the large pores of the separator. Under the high-voltage condition, the electrochemical corrosion attack is intensified by the electrolyte deprotonation reactions,[30] especially on the grains near the separator. The impact of this gradient of CEI thickness on the electrochemical behavior of the thick electrode will be discussed in detail in the following section with the support of computational modeling.

Atomic resolution high-angle annular dark-field imaging (HAADF) was also applied for the cycled lamellas to investigate the phase transformations of primary grains. Although the bulk structure of the bottom grain (close to the current collector) maintains the layered phase after electrochemical cycling, the surface (~2 nm layer in thickness) is transformed to a rock-salt structure as highlighted by the yellow dashed line in Figure 3D. Transition metal ions in bright contrast were found in the Li layer (dark column in HAADF imaging mode) in this surface region, forming the antisite defect layer. In contrast, the whole surface and subsurface regions of the top grain transform to the rock-salt structure, which indicates a low-transition metal out of plane migration barrier. These findings are consistent with a recent report postulating that electrode degradation originates from the cathode surface where point defects and corrosion reactions are abundant.[31] This observed reaction heterogeneity calls for a computational modeling effort to explain the underlying mechanism, which is discussed in the following.

Gradient of CEI thickness and ununiform SOD in thick electrode via computational modeling

From a computational modeling point of view, few reported studies investigated the impact of the CEI. This phenomenon is mainly addressed at the atomic scale

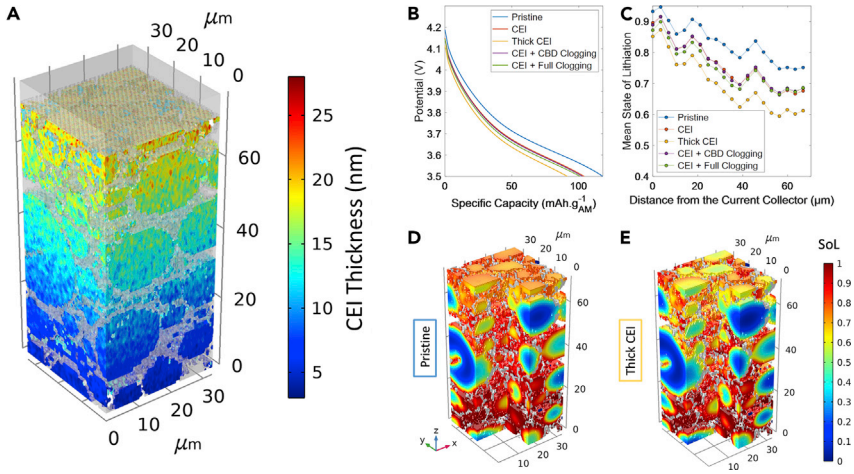

Figure 4. Analysis of CEI impact on SOD in thick electrode via computational modeling

(A) Sub-volume used in the computational model with CEI variation along the electrode thickness direction.

(B) The simulated discharges curves with cutoff voltage at 3.5 V for different CEI thickness and extent of pores clogging.

(C) Distribution of lithiation state along the thickness direction for the NMC811 electrode with a cutoff voltage at 3.5 V for different CEI thickness and extent of pores clogging.

(D and E) 3D distribution of lithiation state with cutoff voltage at 3.5 V for NMC811 electrode without CEI consideration and with thick CEI, respectively.

through density functional theory or molecular dynamics, allowing to unravel the composition of this layer at small time and length scales.[32,33] Recently, an impedance transmission line model was proposed by Scipioni et al. to quantify the resistance due to the CEI based on FIB-SEM images.[34] However, not a single continuum model describing the formation of this layer at the electrode scale is reported in the literature to the authors' knowledge because of the complexity and the lack of solid theory around this phenomenon.

The modeling effort reported in this work does not focus on the Simulation of the CEI formation, but rather on the investigation of its impact at the electrode scale. In our modeling approch the CEI is assumed to have a resistance impacting the overall overpotential (see Table S2). The influence of different CEI formation scenarios on the behavior of the thick electrode were studied during lithiation, starting from a fully delithiated NMC. The contribution of the CEI was captured through a 4D (space + time) electrochemical model already reported by us[35] accounting for an electrode microstructure based on the 3D PFIB-SEM data of the pristine NMC electrode presented earlier in Figure 1B. Then, a sub-volume of 33 × 33 × 70 μm^3 was extracted from these data to be used in the simulations as illustrated in Figure S6. After running an electrolyte impregnation Lattice Boltzmann method model[36] on the sub-volume to assess possible partial wetting due to the low porosity of the electrode (Figure S7), it was found that the electrolyte would wet almost the entirety of the electrode within 40 s after electrolyte injection. In consequence, the void from the PFIB-SEM images was considered to be fully occupied by the electrolyte in the 4D electrochemical model. As mentioned before, different scenarios are compared with a pristine case where the CEI is not considered. The two first cases are the ones with the heterogeneous CEI (called hereafter "CEI") and thick heterogeneous CEI (called hereafter "thick CEI") where its thickness has been doubled. The CEI case represents the electrode after 15 cycles as the electrode presented in the (S)TEM section, while the thick CEI case represents an electrode after a larger number of cycles, as the CEI continues to grow. To capture the

heterogeneity observed experimentally with TEM (Figure 3C), the CEI distribution on Figure 4A was applied to be consistent with the observed heterogeneity at both the electrode and particle levels (more details are available in Figure S8).

Then, as the electrolyte decomposition requires electrons, the reaction is more favorable to occur at the surface of the carbon, which has an electronic conductivity several orders of magnitude higher than the NMC. In the model, the carbon was merged with the binder into the CBD phase to keep the computational cost reasonable. This inactive phase has a microporosity[37] assumed to be fully filled with electrolyte through which the Li^+ ion is free to migrate to reach the surface of the active material to react. If the electrolyte decomposes preferentially on or within the CBD, the formed CEI could clog the pores of the CBD, hindering the ionic transport. To explore this "CBD clogging" scenario, in addition to the CEI layer, the transport of Li^+ ion was blocked through the CBD. Finally, the last hypothesis is that the CEI not only clogs the pores of the CBD but also the narrow gaps between the NMC particles, leading to an increase in the overall tortuosity factor in the electrolyte phase. The "full clogging" hypothesis adds to the CBD clogging one an arbitrarily chosen increase of the tortuosity by a factor of 2, entailing a lower effective diffusion coefficient of Li^+ ions in the electrolyte.

The discharge curves of the 5 different cases at a C/2 rate are represented in Figure 4B with the pristine case displaying the highest specific capacity (120 mAh/g) versus the thick CEI case, which has the lowest specific capacity (92.7 mAh/g) at the cutoff voltage. Interestingly, the CEI, "CEI + CBD clogging" and "CEI + full clogging" cases share a similar discharge capacity around 100 mAh/g. It suggests that the hindered ionic transport does not significantly reduce the performance at this rate for a single discharge. It is noteworthy to mention that the average overpotential between the thick CEI and the "pristine" cases is twice as much as those between the CEI and the pristine cases (79.4 versus 43.8 mV). This overpotential difference can be linked to the additional resistance from the CEI layer, which is two times thicker in the thick CEI hypothesis. However, it is hard to extract more information from this macroscopic observable and that is when the strength of the 3D-resolved modeling comes into play through the access to mesoscale observables. In Figure 4C, the average concentration of lithium in the cross-section plane is plotted as a function of the distance to the current collector at the end of discharge. Once again, the clogging hypotheses do not induce a significant difference when compared with the CEI case, since they have comparable concentration gradients. The steepest gradient is observed for the thick CEI case, while the mildest one is attributed to the pristine case, whose SOD in the upper half (close to the separator) of the electrode is significantly higher. As highlighted in a previous work for solid electrolyte interphase modeling,[38] this accentuated gradient is due to the distribution of the CEI thickness that will favor an intercalation at the bottom (close to the current collector) of the electrode where the CEI is the thinnest. This effect strengthens the electronic insulating nature of the CEI layer, where thicker CEI results in larger charge transfer resistance on the particle surface. As a result, the cell potential for the CEI cases will reach the cutoff voltage faster than the pristine case. In consequence, the system will never reach the point where it becomes more favorable for lithium to intercalate where the CEI is the thickest (near the separator) because the SOD is too high where the CEI is the thinnest (near the current collector). This behavior can be observed through the calculated 3D distribution of the SOD at the end of discharge represented for the pristine and thick CEI cases, respectively, in Figures 4D and 4E. Indeed, in Figure 4D, a milder SOD gradient can be observed along the thickness of the electrode for the pristine hypothesis

Please cite this article in press as: Zhang et al., Coupling of multiscale imaging analysis and computational modeling for understanding thick cathode degradation mechanisms, Joule (2022), https://doi.org/10.1016/j.joule.2022.12.001

compared with the thick CEI in Figure 4E. As reported in Figure 4C, the region with the most difference is the top part, which is poorly utilized in Figure 4E. Moreover, in both cases, strong intraparticle gradients take place in large particles where the solid lithium diffusion is too slow to homogenize the concentration at this rate of intercalation. Moreover, the gradient of concentration along the thickness of the electrode will be exacerbated as the electrode gets thicker. Thanks to discharge simulations at C/3-rate with different electrodes thicknesses, it is shown that even when neglecting the CEI contribution, from a certain thickness a severe drop in performance is observed (Figure S9). All electrodes were stochastically generated and selected based on their transport properties to represent the optimal case for each thickness. Despite these optimal properties, the 240-μm-thick electrode displays a specific capacity ca. 30% lower than the 160- and 80-μm-thick electrodes. It suggests that from a given thickness threshold around 240 μm, these gradients will have a greatly detrimental impact on the performance.

From these simulation results, it transpires that the thickness of the CEI has an impact on the local SOD during the lithiation process. An obvious lithium concentration gradient is expected to occur after the initial charge process once the CEI is formed. This reaction heterogeneity will be exaggerated at higher voltage cutoff when the electrolyte-decomposition-induced CEI becomes thicker. After the discharge, the active material particles with thicker CEI will have lower lithium concentration or equivalently more lithium site vacancies in the structure. Transition metal migration will thus be facilitated when lithium vacancies are present to form spinel/rock-salt-type structure. This hypothesis can well explain the structure transformation heterogeneity at the nanoscale captured through the atomic resolution STEM imaging. Surprisingly, the extent of the clogging of the pores does not appear to have a significant effect on the distribution of the state of lithiation and on the discharge curves. Nonetheless, those hypotheses also impact the discharge of the cell through the ionic transport, i.e., Li^+ ion migration in the electrolyte.

Tortuosity and transport properties in thick electrode via modeling

Flow tortuosity is a key parameter of porous materials that provides a description of the porous structure that can be later utilized in computational models. Accurate characterization of the porous structure is crucial for modeling and predicting the transport properties of the battery materials. PFIB-SEM images capture a larger area, thus providing a more accurate representation of the flow tortuosity of the porous material. In this work, the tortuosity was measured based on the flow velocity vector field, and the process is described in the section of experimental procedures. Table S1 illustrates the computed flow tortuosity based on the reconstructed large volume. The flow tortuosity for the pristine electrode is around 1.5 and does not significantly vary after cycling with different charging cutoff voltage. To visualize the flow tortuosity impact on the transport properties of Li^+ ions, the electrolyte wetting process was simulated for the pristine electrode. As shown in Video S1 and Figure S7, it takes less than 40 s for the electrolyte to wet more than 97% of the pores in the reconstructed volume. Considering the relatively even distribution of the pores in the pristine electrode, this simulation result implies the lithium concentration is invariant along the thickness direction.

The Li^+ ion concentration along the thickness of the electrode for the different CEI cases (and pristine scenario) discussed above was then analyzed to evaluate the transport properties. The cases without pores clogging share a similar Li^+ ion concentration distribution with ca. 8% of difference between the top and bottom of the electrode, while the hypotheses with clogging show stronger gradients along

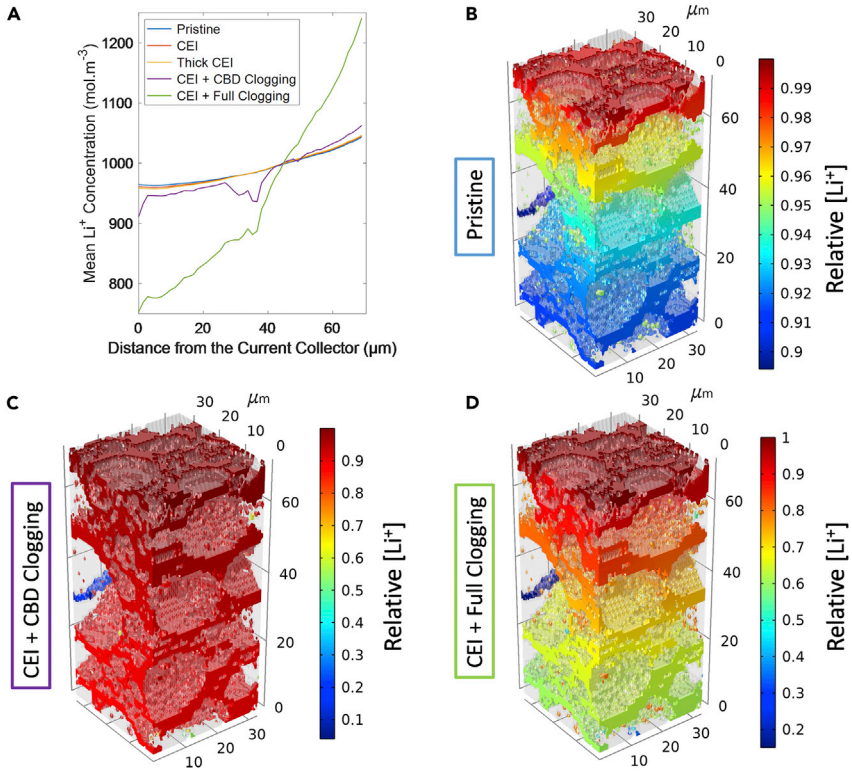

Figure 5. Transport properties analysis in thick electrode via computational modeling

(A) Distribution of lithiation concentration along the thickness direction for NMC811 electrode with cutoff voltage at 3.5 V for different CEI thickness and extent of pores clogging.

(B–D) 3D distribution of lithiation concentration with cutoff voltage at 3.5 V for NMC811 electrode without CEI consideration (B), with CEI and CBD clogging (C), and with CEI and full pores clogging (D).

the thickness, as illustrated in Figure 5A. Indeed, in the CBD clogging case, the difference in Li^+ ion concentration between the separator and the current collector is 15%, while it is around 50% for the full clogging scenario. When comparing the pristine (Figure 5B) to the CBD clogging case (Figure 5C), the latter has regions with very low Li^+ ion concentration. These regions were used to be provided with ions through the CBD microporosity, so when these pores are clogged, Li^+ ion from the bulk cannot feed these regions anymore, and due to the Li^+ ion consumption during intercalation, the concentration drops. The active surface area in these regions will then be lost, entailing a decrease in the specific capacity along cycling. Finally, the full clogging hypothesis in Figure 5D displays the same loss of regions connected to the bulk electrolyte through the CBD, in addition to a stronger gradient along the thickness because of a lower effective diffusion coefficient in the bulk. Despite similar discharge curves after one discharge compared with the CEI case, the clogging of the pores will have an impact on the long-term cyclability of the electrode. Even in the homogeneous sub-volume used in this modeling study, the strong gradient of concentration in the electrolyte will increase along cycling, leading to a higher polarization over time.

The modeling results based on the electrode structure from 3D PFIB data highlight the heterogeneity of the state of lithiation in the thick electrode through an additional charge transfer resistance owing to electronic transport limitations of the CEI. As the CEI will continue to grow along cycling, the electrolyte decomposition

Please cite this article in press as: Zhang et al., Coupling of multiscale imaging analysis and computational modeling for understanding thick cathode degradation mechanisms, Joule (2022), https://doi.org/10.1016/j.joule.2022.12.001

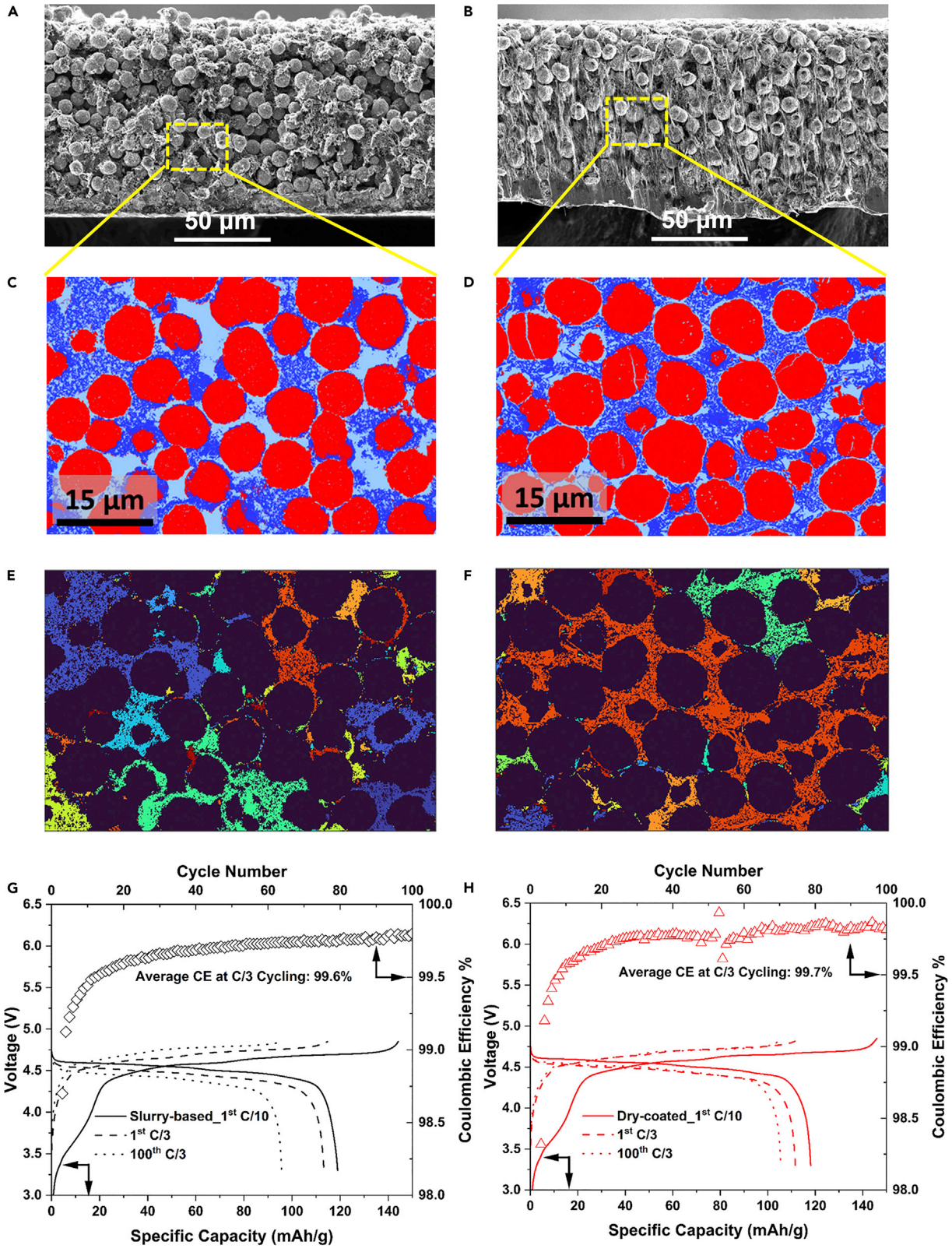

Please cite this article in press as: Zhang et al., Coupling of multiscale imaging analysis and computational modeling for understanding thick cathode degradation mechanisms, Joule (2022), https://doi.org/10.1016/j.joule.2022.12.001

Figure 6. Optimization of CBD network in thick electrode for high voltage cycling stability

(A–H) SEM cross-section image of pristine LNMO thick electrode coated by slurry-based method (A) or dry process (B). The area delimited by the dash line represents the sub-area used in the phase segmentation in (C) and (D). Components segmentation calculated using the PFIB-SEM data for the pristine LNMO thick electrode coated by slurry-based method (C) or dry process (D). The active material is in red, the CBD is in dark blue, and the pores are in light blue. Map of the connected CBD aggregates in the sub-area of the collected PFIB-SEM data for the pristine LNMO thick electrode coated by slurry-based method (E) or dry process (F). Different colors represent different aggregates of connected CBD in both samples. Voltage profiles and cycling CE of LNMO thick electrode coated by slurry-based method (G) or dry process (H) in full cell with graphite as the anode.

could clog the pores of the CBD, eventually hindering Li^+ ion transport. Such reaction heterogeneity will in turn lead to cracks in particles and contact loss between particles and CBD. It also transpires that the architecture of the CBD will play a role in how fast they will be clogged if the CBD is indeed the place where the CEI formation is the most favorable. Therefore, there should be an optimal condition in terms of CBD connectivity to ensure an efficient percolating network for electrons, while keeping the surface area of CBD small enough to prevent electrolyte decomposition.

Optimized CBD percolation network in thick electrode for high voltage cycling stability

Based on the modeling and experimental results above, we employed a dry coating process for thick electrode fabrication for high voltage cycling stability. This dry coating process can enable improved CBD percolation mainly due to the removal of the solvent drying step in the conventional slurry-based coating. Aggregation of CBD can occur during the solvent drying in the slurry-based coating because of convective and capillary force developed in the process.[39] In addition, polytetrafluoroethylene (PTFE) is a widely used binder in the dry electrode, which undergoes a fibrillation process to closely connect both conductive carbon and active materials, while the polyvinylidene fluoride (PVDF) is chosen for the slurry electrode. The CBD morphology in the two cases will be very different with a fiber shape for the dry electrode and an aggregate arrangement for the slurry one. We picked the high-voltage LNMO as the active material to demonstrate the crucial role of CBD in thick electrode since the main obstacle of LNMO commercialization is the instability of CEI.[40] The high operating voltage of LNMO (~4.7 V versus Li^+/Li) exceeds the upper stable voltage limit of the currently commercialized electrolyte, which results in the failure to form an effective passivating layer on the cathode. Consequently, a high areal cathode loading for this type of active material triggers excessive parasitic reactions. Hence, there is a lack of designs reported in the literature to achieve long-term cycling stability for the LNMO thick cathode.

As shown in Figures 6A and 6B, LNMO electrodes (~80 μm in thickness) were fabricated by both conventional slurry-based and dry coating methods. To investigate the CBD percolation network, high magnification PFIB-SEM images were acquired for both electrodes. Based on the PFIB-SEM data, the component segmentation was performed (Figures 6C and 6D), and then, the CBD connectivity maps were built, where each CBD aggregate is in a distinct color (Figures 6E and 6F). From the latter, it transpires that the slurry-based method (Figure 6E) yields more disconnected CBD aggregates, represented by individual colors, with the largest aggregate accounting for only 23.6% of the total amount of CBD. In contrast, in the dry-coated electrode (Figure 6F), the CBD is mainly connected to one large red aggregate representing 57% of the total amount of CBD. The PFIB-SEM images clearly reveal an improved CBD percolation network in the dry-coated LNMO thick electrode owing to the optimized CBD morphology and that the removal of the drying process in the conventional slurry-based coating. To avoid the significant impact from dendrite growth in Li metal anode, graphite anode was used in the full cell to evaluate the cycling

Please cite this article in press as: Zhang et al., Coupling of multiscale imaging analysis and computational modeling for understanding thick cathode degradation mechanisms, Joule (2022), https://doi.org/10.1016/j.joule.2022.12.001

stability of LNMO thick electrodes prepared by both methods. Both electrodes can deliver a high utilization of the active material (~120 mAh/g discharge capacity) at a rate of C/10. When the rate is increased to C/3, the dry-LNMO full cell can achieve 94% capacity retention after 100 cycles, while slurry-based LNMO full cell can only deliver a capacity retention of 84% (Figures 6G and 6H). In addition, the dry-LNMO full cell enables a higher average Coulombic efficiency (CE) (99.7% versus 99.6%) during the cycling at the C/3 rate, which indicates that less parasitic reactions for the CEI formation occur in the dry-coated LNMO electrode. The overpotential as a gauge of cell-level resistance increases obviously in the full cell with slurry-based LNMO electrode along the cycling, which manifests the kinetic limitations of this electrode. These electrochemical performances demonstrate the significance of CBD morphology and percolation network to avoid parasitic reactions and transport limitations in thick electrodes for high voltage cycling stability.

Conclusions

In summary, through a multiscale imaging approach, this study reveals the thick cathode degradation process during electrochemical cycling. This work illustrates the ability of the PFIB-SEM-(S)TEM methods for monitoring microstructure and nanostructure transformations of composite electrodes over large volumes. Such imaging of representative volumes provides the data required for relevant statistical analyses and computational models. It reveals the different root causes of the thick positive electrode degradation over time in a quantitative manner.

First is the cracking of the NMC particles along cycling, with the cracks volume experiencing a relative increase of 24% after 15 cycles, which leads to more electrolyte decomposition to form CEI on the newly exposed surface. In turn, the cracking induces a relative loss of contact between the NMC and the CBD of 20%, weakening the mechanical properties of the electrode and the efficiency of its electronic percolation network.

Second, the CEI contributes to the performance decay, owing to a capacity loss of roughly 10% according to our modeling calculations. The heterogeneity of the CEI is amplified under a high-voltage condition, with the layer being four times thicker near the separator than near the current collector (20 versus 5 nm). Consequently, the lithiation process will also be heterogeneous, favoring the surface area where the CEI is the thinnest. It entails that some regions of the electrode will be submitted to a wider range of lithiation state, leading to higher cracking probabilities. Also, in the hypothesis where the CEI will preferentially be formed at the surface of the carbon additives due to its high electronic conductivity, the micropores of CBD could get clogged. Indeed, the simulations shed light on stronger concentration gradients in the electrolyte and on the loss of active surface area due to more sluggish ionic transport in regions where Li^+ ions used to migrate through the CBD micropores.

This mechanistic understanding of the thick cathode degradation process pinpoints the importance of CBD, which greatly affect the transport networks and cycling stability. The knowledge learned from the thick electrode based on the coupling of multiscale imaging analysis with computational modeling is then applied to thick LNMO electrodes. A dry-coated LNMO cathode with the CBD morphology less prone to clogging is compared with a slurry-based one. The dry-coated LNMO electrode coupled with a graphite anode demonstrates a capacity retention of 94% with a cut-off voltage at 4.85 V, compared with 84% for the slurry-based after 100 cycles. This further proves the validity and value of the conclusions drawn in this work, which can

be used to design better electrode architectures for both current and future generation battery technologies.

EXPERIMENTAL PROCEDURES

Resource availability

Lead contact

Further information and requests for resources should be directed to and will be fulfilled by the lead contact, Ying Shirley Meng (shirleymeng@uchicago.edu).

Materials availability

This study did not generate new, unique reagents.

Data and code availability

Request for the data and analysis codes utilized in this work will be handled by the lead contact, Ying Shirley Meng (shirleymeng@uchicago.edu). Requests about the electrochemical modeling code utilized in this work will be handled by Alejandro A. Franco (alejandro.franco@u-picardie.fr)

Half-cell electrochemical measurements

The commercially available NMC811 cathode is obtained from the Battery500 Consortium and is composed of 95 wt % active material, 2.5 wt % conductive carbon, and 2.5 wt % binder. The cathode laminates were punched into 14-mm diameter discs with mass loading of ~30 mg/cm^2. Lithium metal was used as the counter electrode, Celgard 2325 was used as the separator, and 1 M $LiPF_6$ dissolved in ethylene carbonate (EC)-ethyl methyl carbonate (EMC) with 2 wt % vinylene carbonate (VC) as electrolyte (Gotion, USA). The coin-type cells with 30-μL electrolyte were assembled in an Ar-filled glove box (H_2O < 0.1 ppm). The galvanostatic charge/discharge test was carried out at C/10-rate (1 C = 280 mAh/g) for the initial two cycles in the voltage range of 2.8–4.4 and 2.5–4.7 V, respectively. The cells were then charged and discharged at C/3-rate for the rest of the cycles. All the tests were performed at room temperature. After cycling, the cells were dissembled in the Ar-filled glove box and the cathode were rinsed with DMC solvent to remove salt residues. After drying at room temperature, the cycled cathode materials were stored in the glove box for further characterizations.

Full cell electrochemical measurements

The dry electrode was fabricated via the following procedure. LNMO (from Haldor Topsoe), PTFE binder (from Chemours), and vapor-grown carbon fiber (VGCF, from Sigma Aldrich) were weighed at a mass ratio of 93:2:5. The mixture was then heated to 100°C, followed by a 10-min grinding to obtain a free-standing film. The film was placed on the hotplate and flattened by a stainless-steel cylindrical die at 100°C. Later, the films were hot calendared at 100°C on a 20-μm etched Al foil (from Tob New Energy). The slurry-based LNMO electrode with the same mass ratio for comparison was fabricated following the procedure reported in our previous work.[27] FEI Apreo SEM was used to capture the electrode cross-sections with an acceleration voltage of 5 kV. Electrodes with 12.7 mm diameter were punched and dried in vacuum oven at 100°C for 24 h. Graphite anodes provided by Ningbo Institute of Materials Technology & Engineering (NIMTE) were applied to build the coin-type full cells with the negative to positive electrode capacity ratio (N/P ratio) of 1.1–1.15. Celgard 2325 was used as the separator, and 1-M $LiPF_6$ in EC:EMC = 3:7 wt % from Gotion was used in the full cell testing. In full cell cycling protocols, 1 C is defined as 147 mA/g with a voltage range from 3.3 to 4.85 V. A

Please cite this article in press as: Zhang et al., Coupling of multiscale imaging analysis and computational modeling for understanding thick cathode degradation mechanisms, Joule (2022), https://doi.org/10.1016/j.joule.2022.12.001

rate of C/10 was performed as formation in the first two cycles, followed by C/3 for the rest of the cycles.

Ex situ PFIB-SEM characterization

The PFIB-SEM images were captured by Thermo Scientific Helios UXe PFIB-SEM. As shown in Video S2 and Figure S10, the pristine NMC811 thick electrode with ~85 μm in thickness (~30 mg/cm^2 loading) and 25% porosity after calendering was analyzed using 30 kV Xe^+ ions at a current of 60 nA. The cutting width was 130 μm, and slices were cut every 25 nm. Auto Slice & View 4 (ASV4) software was utilized for automated serial sectioning. The cutting conditions was rocking mill at $\pm 3^\circ$. The signal was then collected in backscattering mode using a retractable circular backscatter detector (CBS) with 2 kV voltage and 200 pA current and active inner rings (a and b rings). The dwelling time for image collection was 1 μs. The original image size was 8,192 × 8,192 voxels (with voxel size of ~ 15.2 × 15.2 nm^2), corresponding to approximately 125 μm horizontal field width. The imaging time was ~84 s for each slice. The imaging was done every 4th slice, giving image the slice thickness of 100 nm, and a total of 330 slices were collected.

The image analysis was performed using Thermo Scientific Avizo software versions 2019.3, 2020.1, and 2020.2. For the results presented here, the analysis was performed on the whole 3D volume. There are four components that are of interest in the sliced image: NMC secondary particles, cracks within the particles, CBD, and pores. Different components were segmented based on a combination of their relative intensity and top-hat segmentation method after a careful denoizing process. Note that pore-back artifacts can cause a portion of pores to appear brighter than the rest and lead to false detection of these regions as CBD.[41] This can undermine the accuracy of the segmentation results, especially in porous materials such as the NMC cathode in this study. A new methodology is applied to correct for pore-back artifacts, which is based on developing an adaptive background mixture model to track and identify voxels that remain relatively unchanged from one slice to the other in a certain axis.

The image-based simulation of tortuosity was performed using XLabSuite extension in the Avizo software. The image-based flow tortuosity simulation requires cubic voxel sizes. Therefore, the images were resampled from 15.2 × 15.2 × 100 nm^3 to 100 × 100 × 100 nm^3, and the analysis was run on the full volume. At the first step, the absolute permeability of the three different samples were measured using the "absolute permeability simulation" module in Avizo. In the next step, the flow velocity vector field that is also generated from the absolute permeability measurement was used to calculate the flow tortuosity. The flow tortuosity is computed using the following formula:

$$\tau_v = \frac{\sum |V|}{\sum V_i}$$

where $|V|$ is the absolute value of local flow velocity and the V_i is the i-component of the velocity in the direction of mean flow.[42]

Ex situ (S)TEM-EDX characterization

FEI Scios DualBeam FIB was used to prepare the lamella samples for STEM imaging. A platinum protecting layer was deposited on the particle before the milling. A gallium ion beam source was used to mill and thin the sample. The operating voltage of the ion beam source was 30 kV. Different emission currents of ion beam were chosen for various purposes, i.e., 5 nA for pattern milling, 10 pA for imaging by ion beam,

and 0.3 nA for cross-section cleaning. The lower operating voltages of the ion beam at 16 and 8 kV were used to thin and clean the lamella. The loading and transfer of the lamella samples to TEM were carefully controlled to prevent air exposure. HRTEM-EDX was recorded on a field emission gun JEOL-2800 at 200 kV with Gatan OneView Camera (full 4 K × 4 K resolution). STEM was performed on JEOL JEM-ARM300CF at 300 kV, equipped with spherical aberration correctors. To minimize possible electron beam irradiation effects, (S)TEM-EDX results presented in this work were acquired under cryogenic temperature. The particle sizes and morphologies were prechecked using the FEI Apreo SEM at an acceleration voltage of 5 kV.

Modeling methodology

The sub-volume used for the computational modeling has a cross-section area of 33 × 33 μm^2 and the full thickness of the segmented volume, i.e., 71.5 μm. The 3D representation for the modeling is available in Figure S6 as well as the component distribution to highlight its homogeneity. The sub-volume was imported into COMSOL Multiphysics as a mesh of ca. 2.3 M of elements using the software INNOV[43,44] to apply our 4D (space + time) Newman-based electrochemical model with the mathematical equations describing Li^+ ion migration in the electrolyte, Li^+ ion insertion driven by Butler-Volmer kinetics, lithium diffusion through the active material and electronic transport in both active material and CBD, similarly to the works previously reported by us.[45,46] A comprehensive description of model parameters and justification for parameters chosen can be found in Tables S2 and S3.

To match with the experimental observations, a heterogeneous CEI thickness (both at the electrode and particle scales) was assumed to exist in the electrode microstructure, ranging from 3 to 28 nm as illustrated in Figure S8. A Gaussian distribution with a mean value that increases along the thickness of the electrode was used to determine the thickness of the CEI layer (additional details are provided in Figure S8). Accounting for the heterogeneity of the CEI layer is of importance, as it has been shown for the anode interphase case that a heterogeneous layer could impact the lithiation process.[38]

SUPPLEMENTAL INFORMATION

Supplemental information can be found online at https://doi.org/10.1016/j.joule.2022.12.001.

ACKNOWLEDGMENTS

UC San Diego's effort is supported by the U.S. Department of Energy's Office of Energy Efficiency and Renewable Energy (EERE) and U.S. Army Tank & Automotive Research Development and Engineering Command (TARDEC) under the award number: DE-EE0008442 (all electrode fabrication, electrochemical testing, and (S)TEM-EDX imaging analysis). PFIB is supported by the funding and collaboration agreement between UCSD and Thermo Fisher Scientific on Advanced Characterization of Energy Materials (PFIB data collection and analysis). The dry LNMO electrode fabrication is supported by the funding and collaboration agreement between UCSD and Chemours. A.A.F., M.C., and A.S. acknowledge the European Union's Horizon 2020 research and innovation programme for the funding support through the European Research Council (grant agreement 772873, "ARTISTIC" project). A.A.F. acknowledges the Institut Universitaire de France for the support. (S)TEM-EDX was performed at the UC Irvine Materials Research Institute (IMRI) using instrumentation funded in part by the National Science Foundation Major Research Instrumentation Program under grant no. CHE-1338173. FIB-SEM was performed in part

at the San Diego Nanotechnology Infrastructure (SDNI), a member of the National Nanotechnology Coordinated Infrastructure, which is supported by the National Science Foundation (grant no. ECCS-1542148). The authors thank Prof. Zhaoping Liu's group from Ningbo Institute of Materials Technology & Engineering (NIMTE) for providing the graphite anode. The authors also want to thank Peter Westenberger from Thermo Fisher Scientific for the discussion on the PFIB image segmentation methods and results.

AUTHOR CONTRIBUTIONS

M.Z. and Y.S.M. designed the experiments. M.Z., M.C., A.A.F., and Y.S.M. performed the mechanism analysis. B.W. and L.L. conducted the PFIB-SEM measurements for pristine and cycled electrodes. A.S., Z.L, R.P., and M.Z. performed PFIB data analysis. S.W. conducted FIB process for TEM lamella samples preparation. M.Z. collected and analyzed *ex situ* (S)TEM images and EDX mapping. M.C., A.S., C.L., and A.A.F. performed the 3D computational modeling and 2D connectivity mapping based on the PFIB data. W.Y. and Y.L. conducted electrode fabrication, electrochemical testing, and SEM data analysis. Y.S.M. and A.A.F. supervised the research. M.Z. and M.C. co-wrote the manuscript. All authors contributed to the discussion and provided feedback on the manuscript.

DECLARATION OF INTERESTS

The authors declare no competing interests.

INCLUSION AND DIVERSITY

We support inclusive, diverse, and equitable conduct of research.

Received: October 3, 2022
Revised: October 23, 2022
Accepted: November 30, 2022
Published: December 22, 2022

REFERENCES

1. Liu, J., Bao, Z., Cui, Y., Dufek, E.J., Goodenough, J.B., Khalifah, P., Li, Q., Liaw, B.Y., Liu, P., Manthiram, A., et al. (2019). Pathways for practical high-energy long-cycling lithium metal batteries. Nat. Energy *4*, 180–186.

2. Singh, M., Kaiser, J., and Hahn, H. (2015). Thick electrodes for high energy lithium ion batteries. J. Electrochem. Soc. *162*, A1196–A1201.

3. Lee, B.-S., Wu, Z., Petrova, V., Xing, X., Lim, H.-D., Liu, H., and Liu, P. (2018). Analysis of rate-limiting factors in thick electrodes for electric vehicle applications. J. Electrochem. Soc. *165*, A525–A533.

4. Li, Z., Yin, L., Mattei, G.S., Cosby, M.R., Lee, B.S., Wu, Z., Bak, S.M., Chapman, K.W., Yang, X.Q., Liu, P., and Khalifah, P.G. (2020). Synchrotron operando depth profiling studies of state-of-charge gradients in thick $Li(Ni_{0.8}Mn_{0.1}Co_{0.1})O_2$ cathode films. Chem. Mater. *32*, 6358–6364.

5. Zan, G., Zhang, J., Monaco, F., Gul, S., Qian, G., Li, J., Vine, D.J., Cloetens, P., Yun, W., Pianetta, P., and Liu, Y. (2021). Understanding multi-scale battery degradation with a macro-to-nano zoom through its hierarchy. J. Mater. Chem. A *9*, 19886–19893.

6. Lu, X., Bertei, A., Finegan, D.P., Tan, C., Daemi, S.R., Weaving, J.S., O'Regan, K.B., Heenan, T.M.M., Hinds, G., Kendrick, E., et al. (2020). 3D microstructure design of lithium-ion battery electrodes assisted by X-ray nano-computed tomography and modelling. Nat. Commun. *11*, 2079.

7. Le Houx, J., and Kramer, D. (2021). X-ray tomography for lithium ion battery electrode characterisation—a review. Energy Rep. *7*, 9–14.

8. Pecher, O., Carretero-González, J., Griffith, K.J., and Grey, C.P. (2017). Materials' methods: NMR in battery research. Chem. Mater. *29*, 213–242.

9. Qian, D., Ma, C., More, K.L., Meng, Y.S., and Chi, M. (2015). Advanced analytical electron microscopy for lithium-ion batteries. NPG Asia Mater. *7*, e193.

10. Li, Y., Cheng, X., Zhang, Y., and Zhao, K. (2019). Recent advance in understanding the electro-chemo-mechanical behavior of lithium-ion batteries by electron microscopy. Mater. Today Nano *7*, 100040.

11. Burnett, T.L., Kelley, R., Winiarski, B., Contreras, L., Daly, M., Gholinia, A., Burke, M.G., and Withers, P.J. (2016). Large volume serial section tomography by Xe plasma FIB dual beam microscopy. Ultramicroscopy *161*, 119–129.

12. Cheng, D., Wynn, T.A., Wang, X., Wang, S., Zhang, M., Shimizu, R., Bai, S., Nguyen, H., Fang, C., Kim, M.-c., et al. (2020). Unveiling the stable nature of the solid electrolyte interphase between lithium metal and LiPON via cryogenic electron microscopy. Joule *4*, 2484–2500.

13. Lee, J.Z., Wynn, T.A., Schroeder, M.A., Alvarado, J., Wang, X., Xu, K., and Meng, Y.S. (2019). Cryogenic focused ion beam characterization of lithium metal anodes. ACS Energy Lett. *4*, 489–493.

14. Smith, N.S., Skoczylas, W.P., Kellogg, S.M., Kinion, D.E., Tesch, P.P., Sutherland, O., Aanesland, A., and Boswell, R.W. (2006). High brightness inductively coupled plasma source for high current focused ion beam applications. J. Vac. Sci. Technol. B *24*, 2902.

Please cite this article in press as: Zhang et al., Coupling of multiscale imaging analysis and computational modeling for understanding thick cathode degradation mechanisms, Joule (2022), https://doi.org/10.1016/j.joule.2022.12.001

15. Kwakman, L., Franz, G., Taklo, M.M.V., Klumpp, A., Ramm, P., Seiler, D.G., Diebold, A.C., McDonald, R., Chabli, A., and Secula, E.M. (2011). Characterization and failure analysis of 3D integrated systems using a novel plasma-FIB system. AIP Conf. Proc. *1395*, 269–273.

16. Luchkin, S.Y., Lipovskikh, S.A., Katorova, N.S., Savina, A.A., Abakumov, A.M., and Stevenson, K.J. (2020). Solid-electrolyte interphase nucleation and growth on carbonaceous negative electrodes for Li-ion batteries visualized with in situ atomic force microscopy. Sci. Rep. *10*, 8550.

17. Wang, M.J., Carmona, E., Gupta, A., Albertus, P., and Sakamoto, J. (2020). Enabling "lithium-free" manufacturing of pure lithium metal solid-state batteries through in situ plating. Nat. Commun. *11*, 5201.

18. Gong, C., Pu, S.D., Gao, X., Yang, S., Liu, J., Ning, Z., Rees, G.J., Capone, I., Pi, L., Liu, B., et al. (2021). Revealing the role of fluoride-rich battery electrode interphases by operando transmission electron microscopy. Adv. Energy Mater. *11*, 2003118.

19. Radin, M.D., Hy, S., Sina, M., Fang, C., Liu, H., Vinckeviciute, J., Zhang, M., Whittingham, M.S., Meng, Y.S., and Van der Ven, A. (2017). Narrowing the gap between theoretical and practical capacities in Li-ion layered oxide cathode materials. Adv. Energy Mater. *7*, 1602888.

20. Lin, F., Nordlund, D., Markus, I.M., Weng, T.C., Xin, H.L., and Doeff, M.M. (2014). Profiling the nanoscale gradient in stoichiometric layered cathode particles for lithium-ion batteries. Energy Environ. Sci. *7*, 3077–3085.

21. Andreu, N., Flahaut, D., Dedryvère, R., Minvielle, M., Martinez, H., and Gonbeau, D. (2015). XPS investigation of surface reactivity of electrode materials: effect of the transition metal. ACS Appl. Mater. Interfaces *7*, 6629–6636.

22. Xu, K. (2014). Electrolytes and interphases in Li-ion batteries and beyond. Chem. Rev. *114*, 11503–11618.

23. Liu, M., Vatamanu, J., Chen, X., Xing, L., Xu, K., and Li, W. (2021). Hydrolysis of $LiPF_6$-containing electrolyte at high voltage. ACS Energy Lett. *6*, 2096–2102.

24. Lee, E.J., Chen, Z., Noh, H.J., Nam, S.C., Kang, S., Kim, D.H., Amine, K., and Sun, Y.K. (2014). Development of microstrain in aged lithium transition metal oxides. Nano Lett. *14*, 4873–4880.

25. Yang, Y., Xu, R., Zhang, K., Lee, S.J., Mu, L., Liu, P., Waters, C.K., Spence, S., Xu, Z., Wei, C., et al. (2019). Quantification of heterogeneous degradation in Li-ion batteries. Adv. Energy Mater. *9*, 1900674.

26. Xue, W., Huang, M., Li, Y., Zhu, Y.G., Gao, R., Xiao, X., Zhang, W., Li, S., Xu, G., Yu, Y., et al. (2021). Ultra-high-voltage Ni-rich layered cathodes in practical Li metal batteries enabled by a sulfonamide-based electrolyte. Nat. Energy *6*, 495–505.

27. Li, W., Cho, Y.G., Yao, W., Li, Y., Cronk, A., Shimizu, R., Schroeder, M.A., Fu, Y., Zou, F., Battaglia, V., et al. (2020). Enabling high areal capacity for Co-free high voltage spinel materials in next-generation Li-ion batteries. J. Power Sources *473*, 228579.

28. Tang, Y., Deng, J., Li, W., Malyi, O.I., Zhang, Y., Zhou, X., Pan, S., Wei, J., Cai, Y., Chen, Z., and Chen, X. (2017). Water-soluble sericin protein enabling stable solid–electrolyte interphase for fast charging high voltage battery electrode. Adv. Mater. *29*, 1701828.

29. Alvarado, J., Schroeder, M.A., Zhang, M., Borodin, O., Gobrogge, E., Olguin, M., Ding, M.S., Gobet, M., Greenbaum, S., Meng, Y.S., and Xu, K. (2018). A carbonate-free, sulfone-based electrolyte for high-voltage Li-ion batteries. Mater. Today *21*, 341–353.

30. Borodin, O., Behl, W., and Jow, T.R. (2013). Oxidative stability and initial decomposition reactions of carbonate, sulfone, and alkyl phosphate-based electrolytes. J. Phys. Chem. C *117*, 8661–8682.

31. Zhang, L., Zhao, C., Qin, X., Wang, S., He, L., Qian, K., Han, T., Yang, Z., Kang, F., and Li, B. (2021). Heterogeneous degradation in thick nickel-rich cathodes during high-temperature storage and mitigation of thermal instability by regulating cationic disordering. Small *17*, e2102055.

32. Borodin, O., Ren, X., Vatamanu, J., Von Wald Cresce, A., Knap, J., and Xu, K. (2017). Modeling insight into battery electrolyte electrochemical stability and interfacial structure. Acc. Chem. Res. *50*, 2886–2894.

33. Xu, S., Luo, G., Jacobs, R., Fang, S., Mahanthappa, M.K., Hamers, R.J., and Morgan, D. (2017). Ab initio modeling of electrolyte molecule ethylene carbonate decomposition reaction on $Li(Ni,Mn,Co)O_2$ cathode surface. ACS Appl. Mater. Interfaces *9*, 20545–20553.

34. Scipioni, R., Isheim, D., and Barnett, S.A. (2020). Revealing the complex layered-mosaic structure of the cathode electrolyte interphase in Li-ion batteries. Appl. Mater. Today *20*, 100748.

35. Chouchane, M., Primo, E.N., and Franco, A.A. (2020). Mesoscale effects in the extraction of the solid-state lithium diffusion coefficient values of battery active materials: physical insights from 3D modeling. J. Phys. Chem. Lett. *11*, 2775–2780.

36. Shodiev, A., Primo, E., Arcelus, O., Chouchane, M., Osenberg, M., Hilger, A., Manke, I., Li, J., and Franco, A.A. (2021). Insight on electrolyte infiltration of lithium ion battery electrodes by means of a new three-dimensional-resolved lattice Boltzmann model. Energy Storage Mater. *38*, 80–92.

37. Daemi, S.R., Tan, C., Volkenandt, T., Cooper, S.J., Palacios-Padros, A., Cookson, J., Brett, D.J.L., and Shearing, P.R. (2018). Visualizing the carbon binder phase of battery electrodes in three dimensions. ACS Appl. Energy Mater. *1*, 3702–3710.

38. Chouchane, M., Arcelus, O., and Franco, A.A. (2021). Heterogeneous solid-electrolyte interphase in graphite electrodes assessed by 4D-resolved computational simulations. Batter Supercaps *4*, 1457–1463.

39. Lombardo, T., Ngandjong, A.C., Belhcen, A., and Franco, A.A. (2021). Carbon-binder migration: a three-dimensional drying model for lithium-ion battery electrodes. Energy Storage Mater. *43*, 337–347.

40. Li, W., Cheng, D., Shimizu, R., Li, Y., Yao, W., Raghavendran, G., Zhang, M., and Meng, Y.S. (2022). Artificial cathode electrolyte interphase for improving high voltage cycling stability of thick electrode with Co-free 5 V spinel oxides. Energy Storage Mater. *49*, 77–84.

41. Prill, T., Schladitz, K., Jeulin, D., Faessel, M., and Wieser, C. (2013). Morphological segmentation of FIB-SEM data of highly porous media. J. Microsc. *250*, 77–87.

42. Koponen, A., Kataja, M., and Timonen, J. (1996). Tortuous flow in porous media. Phys. Rev. E Stat. Phys. Plasmas Fluids Relat. Interdiscip. Topics *54*, 406–410.

43. Chouchane, M., Rucci, A., and Franco, A.A. (2019). A versatile and efficient voxelization-based meshing algorithm of multiple phases. ACS Omega *4*, 11141–11144.

44. Chouchane, M., and Franco, A.A. (2021). An invitation to engage with computational modeling: user-friendly tool for in silico battery component generation and meshing. Batter Supercaps *4*, 1451–1456.

45. Doyle, M., Fuller, T.F., and Newman, J. (1993). Modeling of galvanostatic charge and discharge of the lithium/polymer/insertion cell. J. Electrochem. Soc. *140*, 1526–1533.

46. Doyle, M., Newman, J., Gozdz, A.S., Schmutz, C.N., and Tarascon, J. (1996). Comparison of modeling predictions with experimental data from plastic lithium ion cells. J. Electrochem. Soc. *143*, 1890–1903.